Opto-Electronic Science

ISSN 2097-0382 CN 51-1800/O4

8-nm narrowband photodetection in diamonds

Lemin Jia, Lu Cheng and Wei Zheng

Citation: Jia LM, Cheng L, Zheng W. 8-nm narrowband photodetection in diamonds. *Opto-Electron Sci* **2**, 230010 (2023).

https://doi.org/10.29026/oes.2023.230010

Received: 5 May 2023; Accepted: 27 August 2023; Published online: 27 September 2023

Related articles

Graphene photodetector employing double slot structure with enhanced responsivity and large bandwidth

Siqi Yan, Yan Zuo, Sanshui Xiao, Leif Katsuo Oxenløwe, Yunhong Ding

Opto-Electronic Advances 2022 **5**, 210159 doi: 10.29026/oea.2022.210159

Solvent-free fabrication of broadband WS_2 photodetectors on paper

Wenliang Zhang, Onur Çakıroğlu, Abdullah Al-Enizi, Ayman Nafady, Xuetao Gan, Xiaohua Ma, Sruthi Kuriakose, Yong Xie, Andres Castellanos-Gomez

Opto-Electronic Advances 2023 **6**, 220101 doi: 10.29026/oea.2023.220101

Large-scale and high-quality III-nitride membranes through microcavity-assisted crack propagation by engineering tensile-stressed Ni layers

Jung-Hong Min, Kwangjae Lee, Tae-Hoon Chung, Jung-Wook Min, Kuang-Hui Li, Chun Hong Kang, Hoe-Min Kwak, Tae-Hyeon Kim, Youyou Yuan, Kyoung-Kook Kim, Dong-Seon Lee, Tien Khee Ng, Boon S. Ooi

Opto-Electronic Science 2022 **1**, 220016 doi: 10.29026/oes.2022.220016

In-fiber photoelectric device based on graphene-coated tilted fiber grating

Biqiang Jiang, Yueguo Hou, Jiexing Wu, Yuxin Ma, Xuetao Gan, Jianlin Zhao

Opto-Electronic Science 2023 **2**, 230012 doi: 10.29026/oes.2023.230012

More related article in Opto-Electron Journals Group website

OES Opto-Electronic Science

http://www.oejournal.org/oes

OE_Journal Website

Opto-Electronic Science

Article

July 2023, Vol. 2, No. 7

DOI: 10.29026/oes.2023.230010

8-nm narrowband photodetection in diamonds

Lemin Jia, Lu Cheng and Wei Zheng*

Spectrally-selective photodetection plays a crucial role in various applications, including target imaging and environmental monitoring. Traditional deep-ultraviolet (DUV) narrowband photodetection systems consist of broadband photodetectors and filters, which complicates the architecture and constrains imaging quality. Here, we introduce an electronic-grade diamond single-crystal photodetector exhibiting an exceptionally narrow spectral response in the DUV range with a full width at half maximum of 8 nm. By examining diamond photodetectors with varying dislocation densities, we propose that mitigating the defect-induced trapping effect to achieve charge collection narrowing, assisted by free exciton radiative recombination, is an effective strategy for narrowband photodetection. The superior performance of this device is evidenced through the imaging of DUV light sources, showcasing its capability to differentiate between distinct light sources and monitor human-safe sterilization systems. Our findings underscore the promising potential applications of electronic-grade diamond in narrowband photodetection and offer a valuable technique for identifying electronic-grade diamond.

Keywords: narrowband photodetection; electronic-grade diamond; charge collection narrowing

Jia LM, Cheng L, Zheng W. 8-nm narrowband photodetection in diamonds. *Opto-Electron Sci* **2**, 230010 (2023).

Introduction

Photodetectors are the mainstay of sensing and imaging systems[1–5], which can be classified into the types of broadband[6–10] and narrowband[11,12] according to spectral response width, between which the latter one is increasingly demanded in industrial and scientific research fields due to the spectral resolution capability. In general, conventional inorganic semiconductor photodetectors have a significant response in a large spectral range with energy greater than the band gap of active layer, such as silicon diodes, whose response spectra cover the range from near-infrared to ultraviolet (UV)[13–16]. Therefore, a common approach to achieve narrowband photodetection of specific wavelengths is combining broadband photodetectors with band-pass filters[17,18]. However, this approach faces three challenges, including decreased sensitivity of the photodetector, increased structural complexity and cost, and a lack of filters available for shorter wavelength ranges. Under this circumstance, the concept of charge collection narrowing (CCN) can provide a new strategy to realize narrowband photodetection[11]. The working principle of CCN devices is to narrow charge collection efficiency into the desired spectral region, that is, designing device structure (such as the thickness of absorber layer) to ensure that only bulk charge generated by the incident wavelength near optical bandgap will be collected while the surface charge generated by shorter wavelength will not, which is a generic and architecture-driven process in essence[11]. Mechanisms behind the methods of optoelectronic manipulation need to be carefully investigated especially for materials with different light absorption and charge transport properties. To date, only the narrowband photodetectors based on organic semiconductor or perovskite materials have been successfully demonstrated through efficient optoelectronic manipulation methods in infrared, visible and near UV spectral ranges[12,19–21]. Filterless narrowband photodetection based on wide-bandgap

State Key Laboratory of Optoelectronic Materials and Technologies, School of Materials, Sun Yat-sen University, Shenzhen 518107, China.
*Correspondence: W Zheng, E-mail: zhengw37@mail.sysu.edu.cn
Received: 5 May 2023; Accepted: 27 August 2023; Published online: 27 September 2023

Open Access This article is licensed under a Creative Commons Attribution 4.0 International License.
To view a copy of this license, visit http://creativecommons.org/licenses/by/4.0/.

© The Author(s) 2023. Published by Institute of Optics and Electronics, Chinese Academy of Sciences.

inorganic semiconductors in deep-UV (DUV) spectral range is highly anticipated in the fields of optical communication, environmental monitoring, lithography, and space exploration[22–25].

Among the wide-bandgap semiconductor materials, diamond is an ideal candidate for DUV photodetectors that can withstand harsh environments due to excellent properties such as high carrier mobility and saturation velocity, large breakdown electric field, high chemical inertness, and thermal stability[26–28]. Achieving the optoelectronic manipulation of diamond for narrowband response can further improve detection precision and accuracy, which is of great significance to meet the application needs from specific wavelength bands. As is known, the spectral response of a photodetector depends on carrier mobility and the lifetime of photogenerated carriers under excitation at different wavelengths[29]. Therefore, for semiconductors with low mobility such as organic ones, increasing sample thickness is an effective strategy to achieve CCN[11]. However, for diamonds with high mobility, simply increasing the thickness will not significantly reduce the collection of photogenerated carriers under shortwave excitation, which makes carrier lifetime an important parameter and factor to be considered. The trapping effect of trap levels on carriers caused by dislocations in diamond can significantly increase the lifetime of carriers and enhance the photoconductive output of devices[24], which may explain the broadband response exhibited by reported photodetectors based on thick diamond single-crystal[27] to some extent.

Following this idea, an electronic-grade diamond-based DUV narrowband photodetector with a peak external quantum efficiency (EQE) of 228 nm and a spectral response with the full width at half maximum (FWHM) of less than 8 nm is prepared. Research on diamond photodetectors with different dislocation densities demonstrates that two physical processes of free exciton (FE) radiation recombination[30] and defect-induced traps determine the steady-state distribution of photogenerated carriers under excitation at different wavelengths[31], which thus plays a key role in spectral response width. The as-prepared narrowband photodetector exhibits extremely low dark current due to low defect density, resulting in a high specific detectivity (D^* ~10^{13} Jones) and a compliant linear dynamic range (LDR~118 dB). With germicidal UV light sources as an example, the spectrally-resolved imaging capability of this photodetector is presented.

Results and discussion

Diamond single-crystal narrowband photodetectors

Three diamond single crystals respectively named A, B, and C with different defect states are studied here (see Methods for details). The thicknesses of diamonds A, B, and C are 680 μm, 680 μm, and 780 μm, respectively. Among them, diamond A is an electronic-grade diamond with extremely high purity. X-ray diffraction is an efficient method to detect poloidal and azimuthal spreads (tilts and twists) of the layer induced by dislocations. Screw and edge dislocation densities can be extracted from symmetric and asymmetric ω-scans, respectively[32,33]. Figure 1(a) shows the X-ray rocking curves of (111) and (004) planes of diamond A, whose FWHM is 25.7 and 28.9 arcsec, respectively, with the screw and edge dislocation densities calculated as 5.7 ×10^5 cm^{-2} and 3.6 × 10^5 cm^{-2}. Insets shown in this figure are φ-scans of the (111) plane at different χ (50°–60°), where the reflection peaks repeat at every 90° with the signals appearing within a small range of χ angles. ϕ is the lattice plane inclination, whose narrow FWHM also reflects the good figure of merit of twist. The FWHM of Raman spectrum of only 1.76 cm^{-1} indicates a fairly-high degree of lattice perfection and a low amount of residual stress[34] (Fig. 1(b)).

Structure schematic diagram of the device based on diamond A is shown in Fig. 1(c) (see Methods). As light entered from the top of crystal, photogenerated electrons and holes would drift through the crystal under an applied electric field and then got collected by the electrodes at both ends to output a photocurrent. Since light below 200 nm will be strongly absorbed by air, all optoelectronic tests were carried out under vacuum conditions and reverse bias to obtain complete response spectra of the device. The EQE spectra of two devices numbered 1, 2 and based on diamond A (two identical diamonds grown under the same condition) are shown in Fig. 1(d) where the insets are photographs of these two devices. An interesting phenomenon is observed that the EQE spectra of both devices exhibit a narrow peak centered around 228 nm with FWHMs of less than 8 nm near the absorption edge. Although photoresponse also exists in the shorter wavelength range up to 167 nm, the responsivity shown in inset exhibits a drop of more than one order of magnitude compared to the peak response in short wavelength range. Limited by the transmittance of top electrode (Fig. S1), the maximum EQE values of

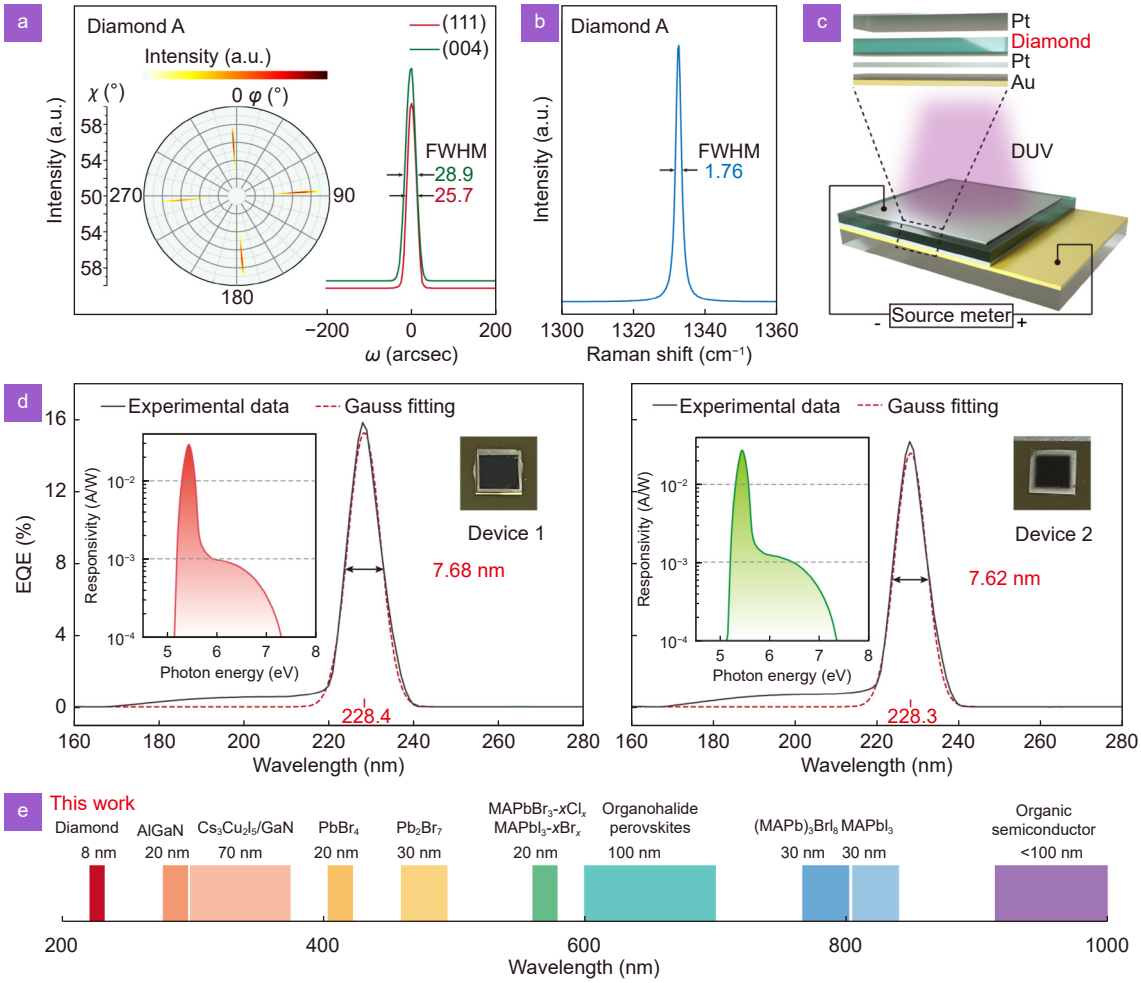

Fig. 1 | Device structure and narrowband photodetection of electronic-grade diamond A-based photodetectors. (**a**) X-ray rocking curves of (111) and (004) planes of diamond A. Insets are ϕ-scans of the (111) plane at different χ (50°–60°). (**b**) Raman spectrum of diamond A. (**c**) Schematic diagram of the device structure. (**d**) EQE spectra of Device 1 and Device 2 based on diamond A, where extremely narrow EQE peaks have been shown. Insets are corresponding optical photographs and responsivity spectra with photon energy as abscissa. (**e**) The performance of typical narrowband photodetectors over the entire spectral range with the diamond device showing the shortest detection wavelength and narrowest EQE peak.

Device 1 and 2 at 1 V bias voltage are 15.8% and 14.7%, respectively. The device performance was essentially unchanged after one month (Fig. S2). Besides, compared with currently-reported narrowband photodetectors across the entire spectral range (some typical reports are listed in Fig. 1(e) and Table 1)[12,19–21,35–39], the diamond A-based photodetector prepared here has shown the shortest detection wavelength and narrowest EQE peak.

Mechanism of narrowband photodetection

As shown in Fig. 2(a), for diamond A with low dislocation density, the main physical processes of photodetection[40,41] include the absorption of photons (with an energy greater than band gap) to excite electrons from the valence band to the conduction band or higher-energy excited states (which are finally relaxed to the bottom of conduction band via phonon emission and other processes), after which freely-movable electrons will be generated in the conduction band and freely-movable holes will be left in the valence band. Then, photoconductive signals can be induced under an electric field (1), or radiative recombination will be generated via localized energy states in the forbidden band (2). It should be noted that practical physical processes occurring in crystals under optical excitation are much more complex, and only a few dominant ones will be discussed here in detail with other non-radiative recombination processes ignored temporarily. Specifically, the analysis of radiative recombination was conducted through photoluminescence (PL) spectroscopy, while the analysis of non-equilibrium

Table 1 | Performance of representative narrowband photodetectors in the range from infrared to ultraviolet.

Materials	λ_{peak} (nm)	FWHM (nm)	V_{bias} (V)	EQE (%)	References
SQ-H:$PC_{61}BM$	1050	~85	0	12.3	ref.[19]
$MAPbI_3$	830	~33	5	10^4	ref.[35]
$MAPbI_3$/PCBM	800	29	0	9.9	ref.[36]
Pb_5I_{16}	690	60	5	200	ref.[37]
$CH_3NH_3PbI_2Br$_Rhodamine B	650	<100	–0.5	10	ref.[12]
$MAPbBr_3$	570	<20	–4	3	ref.[20]
$PbI_{1.4}Br_{0.6}$_PEIE	450	<100	-0.5	10	ref.[12]
$MAPbI_2Br$/Spiro-OMeTAD	350	80	0	40	ref.[21]
$Cs_3Cu_2I_5$/GaN	320	70	0	—	ref.[38]
AlGaN	275	~20	–5	89	ref.[39]
Diamond	228	~8	–1	15.8	This work

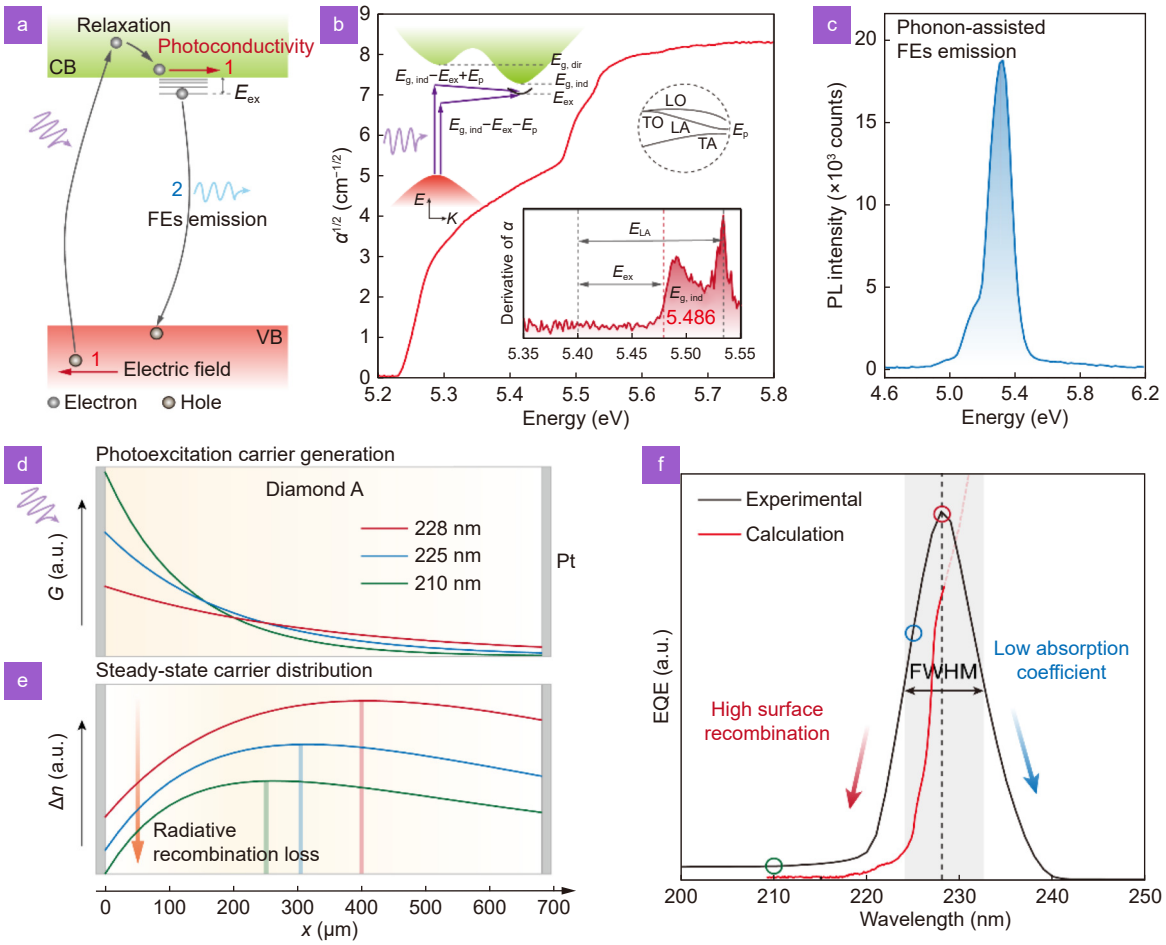

Fig. 2 | Narrowband photodetection mechanism based on diamond A. (**a**) Schematic diagram of main physical processes occurring in diamond A under photoexcitation. (**b**) Absorption spectrum of diamond A. The inset shows a schematic diagram of absorption process and a differential spectrum of absorption coefficient. (**c**) PL spectrum of diamond A under 193 nm pulse excitation. (**d**) and (**e**) Spatial distribution of photoexcited excess carrier generation rate G and steady-state carriers within the device. The three selected wavelengths are 210 nm, 225 nm, and 228 nm. (**f**) Experimental EQE and simplified-calculated EQE of the diamond A-based photodetector with the three selected wavelengths marked. This simplified model can well explain the decline of EQE at shortwave.

carrier lifetime was performed using voltage signal measurements under pulsed light excitation.

Figure 2(b) shows the absorption spectrum of diamond A, which reflects corresponding energy states in the crystal and the transition process between them (the ordinate of $\alpha^{1/2}$ is to make the image of absorption edge

clearer). A sharp boundary of the absorption onset indicates a low-energy state between the top of valence band and the bottom of conduction band, which further proves the low density of defect states owned by diamond A[42]. As an indirect-bandgap semiconductor, the absorption coefficient of diamond is a joint contribution of exciton structure state and four phonons (TA, LA, TO, LO), as shown in the inset. Inset in Fig. 2(b) shows the differential spectrum of α, where the band gap of diamond A is calculated to be 5.486 eV (exciton binding energy E_{ex}~80 meV) approximately by the assignment of exciton absorption of emitting LA phonons (127 meV)[43–45]. The essence of exciton radiative recombination luminescence of diamond is actually the inverse process of exciton absorption. Figure 2(c) exhibits the photoluminescence (PL) of diamond A under 193 nm pulse excitation, where an ultra-intense free exciton emission is observed with the peak in a certain width is found[46]. This is attributed to the involvement of numerous phonons at room temperature, preventing the detailed identification of specific phonon-assisted excitonic emission processes. This result demonstrates that exciton emission is the dominant recombination process under photoexcitation.

The steady-state distribution of carriers within a crystal under photoexcitation will directly affect the photoconductive output of devices, which is jointly determined by photoexcitation, diffusion, and recombination processes[31]. As shown in Fig. 2(d), the spatial distribution of photoexcited excess carrier generation rate G within the sample decays exponentially in accordance with the Beer-Lambert law[47], that is, $G \propto \alpha e^{-\alpha x}$ (thickness d of diamond A is 680 μm). Three selected characteristic wavelengths are 228 nm, 225 nm and 210 nm respectively with corresponding EQEs shown in Fig. 2(f). It can be observed that light at 228 nm decays slowly with depth, which can penetrate the crystal and generate photogenerated carriers inside. As the wavelength decreases, photoexcited carriers generated are more concentrated on the surface, of which the low penetration depth of light at 210 nm can be an example. Obviously, photogenerated carriers generated present a non-uniform distribution inside the crystal, which thus will diffuse into the interior for equilibrium. What's more, all radiative and nonradiative recombination processes can lead to an annihilation of carriers and thus reduce carrier concentration. Considering the effect of surface recombination and taking electrons as an example, the steady-state distribution of photogenerated carriers can be expressed as[48]:

$$\Delta n = J\frac{\alpha d^2/D_e}{1-\alpha^2 d^2}\left\{e^{-\alpha x} - \left(\frac{\alpha d + sd/D_e}{1+sd/D_e}\right)e^{-x/d}\right\}, \quad (1)$$

where J is a constant related to incident light flux and reflectivity; D_e is the electron diffusion coefficient related to mobility; s is the surface recombination velocity proportional to the excess carrier concentration at surface. According to that, the spatial distribution of charge carriers excited at different wavelengths in the crystal can be obtained (Fig. 2(e)). As the wavelength decreases, the carrier concentration in crystal gradually decreases, and the maximum value of entire concentration moves toward the surface. In addition, a strong absorption near the surface can lead to a stronger radiative recombination, which thus brings a significant increase in surface recombination velocity. On this basis, an ideal simplified case is considered here, that is, assuming diamond A as a perfect crystal with the influence of all defect energy levels neglected. Besides, the surface recombination velocity is considered to be so high[49] that $sd/D_e \gg 1$. Under the condition of $\alpha d \gg 1$, the photoconductivity of a device can be expressed as[48]:

$$\Delta G = AJ\frac{e}{d^2}(\mu_n\tau_n + \mu_p\tau_p)\left(\frac{1}{\alpha L_D} + \frac{D_e}{sd}\right), \quad (2)$$

where A is the illuminated area, μ_n and μ_p the electron and hole mobility, respectively, τ_n and τ_p the electron and hole lifetime, respectively, and L_D is the bipolar diffusion length depending on $\mu_n\tau_n$ and $\mu_p\tau_p$. It can be observed from this formula that the change of ΔG with excitation wavelength mainly depends on the factor $\left(\frac{1}{\alpha L_D} + \frac{D_e}{sd}\right)$, where L_D, D_e and d all can be regarded as constants. Clearly, both α and s will increase with decreasing wavelength to cause a significant drop in photoconductivity. As shown in Fig. 2(f), the red line represents the EQE calculated according to this formula as a function of wavelength (the simplified calculation here is to illustrate the changing trend with absolute values actually being meaningless).

To sum up, the narrowband response of diamond A-based photodetectors can be well explained as follows: In the region of low absorption coefficient, photogenerated carriers can be excited throughout the crystal to be collected by electrodes under an electric field. As wavelength decreases, the gradually-increasing absorption coefficient results in a significant increase in photoresponse. This mechanism is well-known in the

context of photodetectors. After reaching the peak of response, as wavelength continues to decrease, photogenerated carriers generated will be more concentrated on crystal surface, which are mainly annihilated through the radiative recombination process rather than being transmitted to the back of crystal and collected by the electrodes, thus leading to a significant drop of photoresponse in the shortwave region (see Fig. S3 for schematic diagram).

Analysis above concludes that the strong radiative recombination and short carrier lifetime caused by low dislocation density are the key factors for realizing narrowband photodetection. To further demonstrate this point, photodetectors with the same structure but based on diamonds B and C are also studied here. For two diamonds, the FWHMs of rocking curves on (004) planes are 34.9 and 39.3 arcsec, and the calculated edge dislocation densities are 5.2×10^5 cm^{-2} and 6.6×10^5 cm^{-2}, respectively[32,33] (Fig. S4). The FWHMs of Raman peaks are 1.89 cm^{-1} and 2.16 cm^{-1}, which are consistent with what's shown by rocking curves (Fig. S4). Infrared absorption spectra further assigned impurity absorption of diamond B and C (Fig. S5). The band gaps extracted by absorption spectra are 5.493 eV and 5.490 eV, respectively[43], and an obvious tailing of absorption edge of diamond C proves the existence of defect states[50] (Fig. S6). From Fig. 3(a) an interesting phenomenon unlike that of diamond A is observed that the photoresponse of diamonds B and C exhibits distinct shapes without showing narrow peaks with corresponding FWHMs at 31 nm and 52 nm, respectively. For crystals with higher dislocation density, the defect states will increase significantly. Therefore, as shown in Fig. 3(b), the main physical processes in crystals under photoexcitation, in addition to the previously-described processes (1) and (2), also involve the donor-acceptor pair radiative recombination transition process (3) and carrier trapping process (1')[50]. Like process (2), process (3) is radiative recombination that can lead to carriers' annihilation, whereas process (1') increases the lifetime of carriers and thus enhances photoconductive signal. The radiative recombination process is measured by PL spectroscopy (Fig. 3(c)). Compared with diamond A, the exciton emission intensity of diamonds B and C decreases sequentially. In addition, diamond B also has defect luminescence in the visible light range, proving the existence of process (3). The carrier lifetime is measured by the transient excitation voltage response of the device under an electric field (Fig. 3(d)). As expected, diamond A has the shortest carrier lifetime, confirming the rapid annihilation process of carriers through radiative recombination; diamond C has the longest lifetime more than tens of times that of diamond A, demonstrating a significant carrier trapping effect within the crystal, which is attributed to the larger density of trap states in this diamond. It should be noted that the comprehensive identification of specific defect states within diamond is a highly intricate process. Currently, numerous researchers are still engaged in related research efforts. Therefore, in this paper, we solely provide a qualitative analysis to elucidate the mechanism.

Further, diamond C is taken as an example to elucidate the broadband response mechanism of diamonds with a higher density of trap states. Fig. 3(e) shows the spatial distribution of G in diamond C (thickness of 780 μm) with typical photoexcitation wavelength as 220 nm and 205 nm, and the corresponding EQEs are shown in Fig. 3(g). Apparently, the distribution of excess carrier generation rates under excitation at these two wavelengths is similar, which is caused by the similar absorption coefficients. Based on PL spectrum and transient excitation voltage response of diamond C, since photogenerated carriers contribute more to process (1') rather than process (2), a simplified case that ignores the surface recombination of diamond is considered here with the Eq. (1) being simplified into $\Delta n = J\frac{\alpha d^2/D_e}{1-\alpha^2 d^2}(e^{-\alpha x} - \alpha d e^{-x/d})$[48], based on which the resulting steady-state distribution of photogenerated carriers is shown in Fig. 3(f). It can be found that the carrier distribution under excitation at 205 nm is similar to that at 220 nm, but the overall carrier concentration of the former is slightly larger. On the premise of ignoring surface recombination effects, the photoconductivity can be simplified as $\Delta G = AJ\frac{e}{d^2}(\mu_n\tau_n + \mu_p\tau_p)(1-e^{-\alpha d})$[48]. The EQE calculated based on this formula is shown as the red line in Fig. 3(g), showing a trend consistent with the experimentally-measured EQE.

Above all, the broadband response of diamond C-based photodetector can be well explained as follows: the high dislocation density of diamond C leads to more trap states in crystal, which gets carriers trapped and thus with long lifetime. Even under an excitation from shorter-wavelength light, although carriers are generated close to the surface, they can still diffuse into the crystal interior due to less radiative recombination. Also, because of the long carrier lifetime, these carriers can be collected

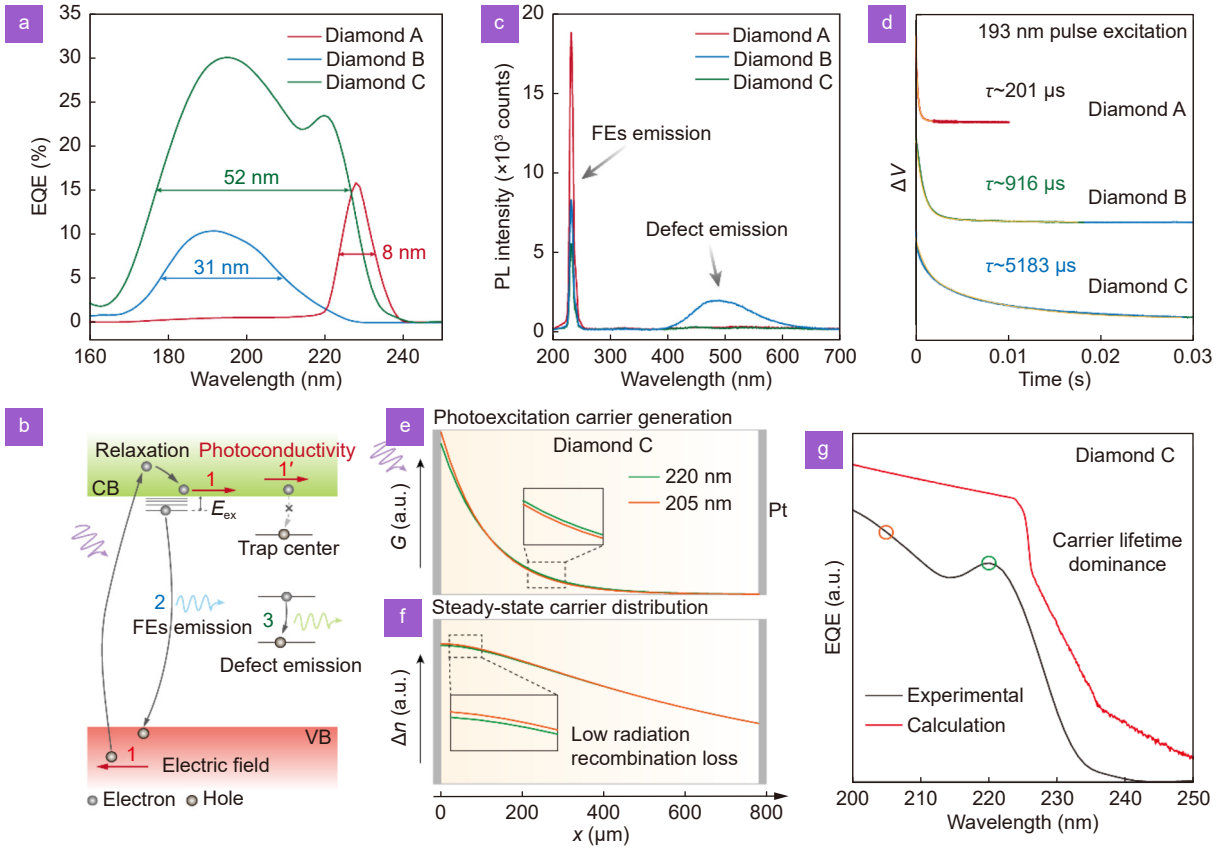

Fig. 3 | Broadband photodetection mechanism based on diamonds B and C. (**a**) EQE comparison of photodetectors based on diamonds A, B, and C. (**b**) Schematic diagram of main possible physical processes of diamonds B and C under photoexcitation. (**c**) PL spectra of diamonds A, B, and C under 193 nm pulse excitation. (**d**) Voltage signals (Δ*V*) of photodetectors based on diamonds A, B, and C under 193 nm pulse excitation. Lifetime of 201 μs, 916 μs, and 5183 μs can be obtained by falling edges, respectively. (**e**) and (**f**) Spatial distribution of photoexcited excess carrier generation rate *G* and steady-state carriers within diamond C-based device. The two wavelengths selected are 205 nm and 220 nm, respectively. (**g**) Experimental EQE and simplified calculated EQE of the diamond C-based photodetector with a consistent trend shown between.

by the back electrodes in electric field, which will not lead to a decrease of photoresponse (see Fig. S7 for schematic diagram).

Performance of narrowband photodetectors

To evaluate the photodetection capability of diamond-based narrowband photodetectors, systematic performance tests are carried out. Figure 4(a) shows the dark current and responsivity of a device under illumination with different wavelengths. Due to the extremely low defect density of diamond A, this device shows an extremely low dark current (I_d). For example, the dark current is less than 10^{-13} A at a bias voltage of 10 V. The responsivity of the device under an irradiation at 228 nm is more than an order of magnitude higher than that at 185 nm at different bias voltages. Assuming that the noise in the device primarily originates from dark current, the detectivity under 1 V bias can be calculated by the formula $D^* = \frac{\lambda e\sqrt{A}EQE}{hc\sqrt{2eI_dB}}$ (λ is the wavelength, B is the bandwidth, e is the elementary charge, h is the Planck's constant, and c is the speed of light)[51], as shown in Fig. 4(b). A high D^* (>10^{12} Jones) exhibited in the response band at room temperature benefits from low shot noise. Figure 4(c) shows the linear dynamic range (LDR) of 118 dB of the device at 1 V bias according to LDR =20×log (I_p/I_d), where I_p is the photocurrent. Furthermore, under an irradiation with different optical powers, the device can repeatedly generate stable photocurrent and dark current, as shown in Fig. 4(d). As bias voltage increases, a more significant increase is exhibited by the responsivity in shortwave region, which is because the enhancement of electric field increases the drift length of photogenerated carriers and thus allows more charges to be collected by the electrodes (Fig. 4(e)). The performance of this device has been further studied at high temperature (Fig. 4(f)). Under an irradiation at 228 nm, the photocurrent of this

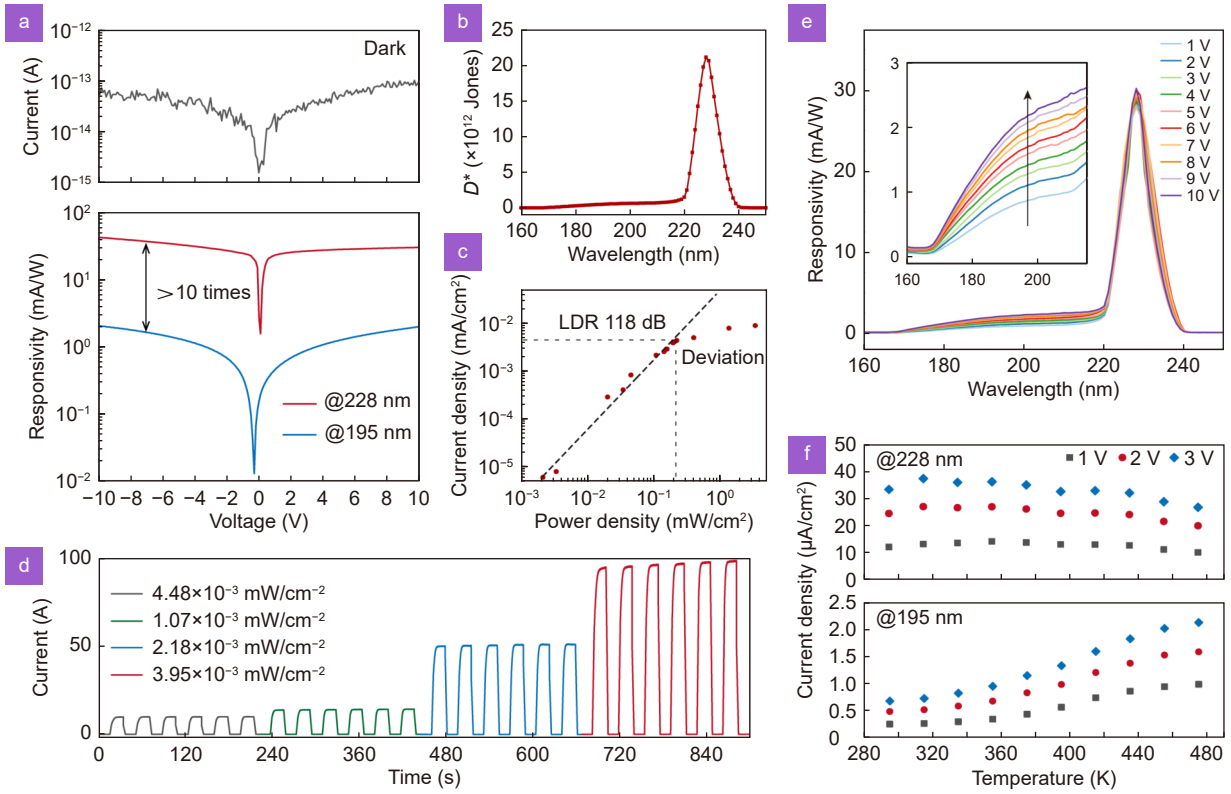

Fig. 4 | Performance of narrowband photodetectors based on diamond A. (**a**) Dark current and responsivity at different bias under 228 nm and 185 nm irradiation. (**b**) Specific detectivity (D^*) spectrum under 1 V bias. (**c**) Linear dynamic range (LDR) of the device under 1 V bias and 228 nm irradiation. (**d**) Temporal response under 1 V bias and 228 nm irradiation with different optical powers. (**e**) Responsivity spectra under 0-10 V bias. The inset is an enlarged view of the shortwave region. (**f**) Measurements on varying temperatures of the device under 0–3 V bias. Different trends are exhibited under 228 nm and 185 nm irradiation.

device shows a slight downward trend with increasing temperature, which may be caused by a slight decrease in mobility due to higher temperature. However, under an irradiation at 185 nm, the photocurrent increases significantly with higher temperature, which indicates the dominant role increasing temperature plays in the increase of carrier lifetime[52]. These results further demonstrate the narrowband response mechanism mentioned above. Furthermore, the fact that the device exhibits a rise time of only 3 μs demonstrates its rapid response speed (Fig. S8).

The device's imaging was demonstrated for different DUV light sources, including a 222 nm excimer lamp and a low-pressure mercury lamp (see Fig. S9 and Methods). Figure 5(a) shows an optical photograph of the excimer lamp. The photosensitive area of the device is 500 μm × 500 μm (ie. pixel size). According to the image plotting the output current of this device at different positions in Fig. 5(b) (65 × 22 pixels), this detector can be aligned with excimer lamp for clear imaging. The radiation spectrum of this excimer lamp is shown in Fig. 5(c) with the peak wavelength of 222 nm having been proven harmless to human body and thus able for sterilization and radiation therapy on body surface[53]. A partial overlap found between the lamp spectra and the EQE indicates the ability owned by this device to well detect and image this light source. Relevant studies of the low-pressure mercury lamp are exhibited in Fig. 5(d–e), including an optical photograph and corresponding scanned images. Spectral lines of this low-pressure mercury lamp mainly include 185 nm, 194 nm, and 254 nm (Fig. 5(f)), among which the first two can produce ozone in the air and thus harm human health, and the last one can cause irreversible damage to human skin and eyes, which is often used for sterilization and disinfection in indoor environments[53]. Since there is only a little overlap between these spectral lines and the EQE, mercury lamps cannot be imaged. These results show that the prepared device can distinguish two UV light sources well.

Conclusion

In summary, we have demonstrated narrowband

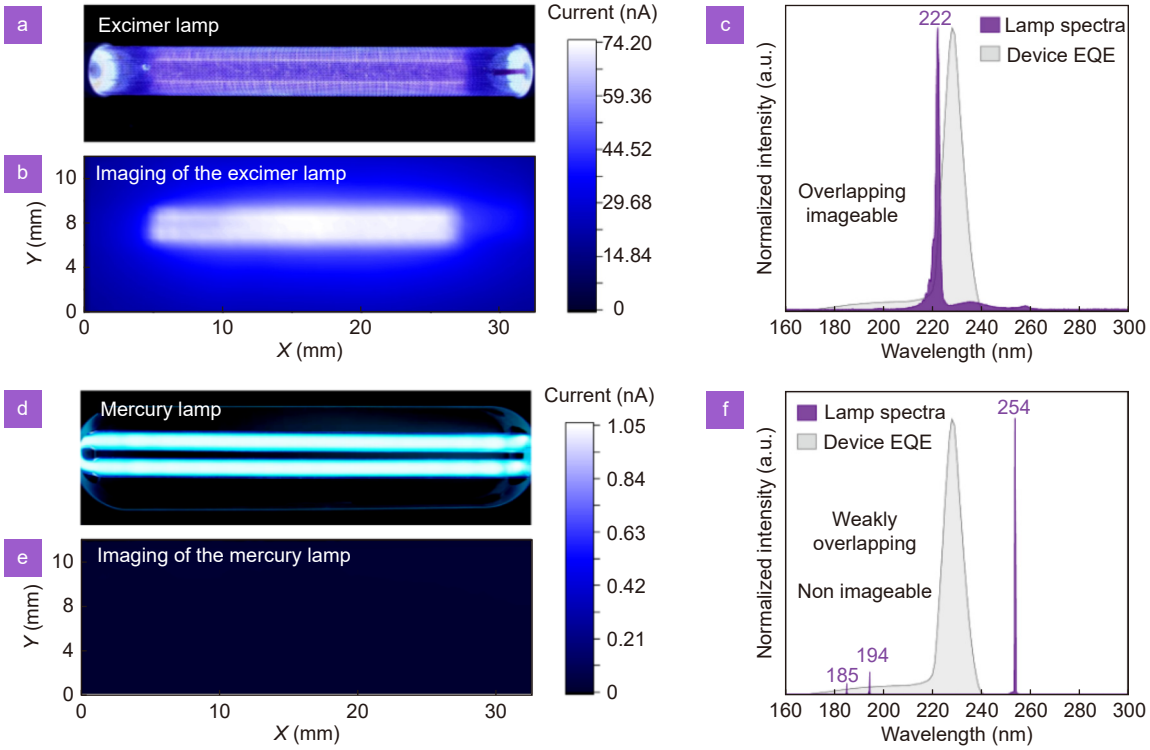

Fig. 5 | Imaging demonstration of narrowband photodetectors for DUV light sources. (**a**) Photograph of 222 nm excimer lamp. (**b**) Imaging of the device for excimer lamp with a size of 65 × 22 pixels whose size is 500 μm × 500 μm. (**c**) Normalized excimer lamp spectrum and EQE of the device, where an overlap can be observed. (**d**) Photograph of mercury lamp. (**e**) Imaging of the device for mercury lamp. (**f**) Normalized mercury lamp spectrum and EQE of the device, where only a weak overlap is found.

photodetection of electronic-grade diamond single-crystal photodetectors. Through a comparison of several diamond-based devices with different dislocation densities, it can be concluded that the suppression of shortwave excitation charge collection by surface radiative recombination leads to narrowband photodetection. For diamonds with high mobility, shortening carrier lifetime can be an effective method to achieve narrowband photodetection. The as-prepared narrowband detector shows an ultra-narrow EQE peak, extremely low dark current, and high light-dark rejection ratio, whose application potential has been demonstrated by preliminary imaging presentation. The practical performance of this detector can be further improved by fabricating area array devices and optimizing device structure. On the other hand, the narrowband response of diamond A distinguishes it from other diamonds, indicating that the spectral response test of diamond is a feasible method to identify whether it is an electronic-grade diamond.

Methods

Materials and characterization

Diamond A is a CVD single crystal commercially purchased from Element Six Co. Ltd. Diamond B was synthesized by high-temperature and high-pressure (HTHP) temperature gradient method (5.5 GPa, 1450 °C). Diamond C was synthesized by microwave plasma chemical vapor deposition (MPCVD) method with raw materials of H_2, CH_4, and O_2. High-resolution XRD was obtained via an Empyrean smart X-ray diffractometer, including ω-scans and φ-scans. Raman spectra were measured via Horiba LabRam HR Evolution confocal Raman Microscope System with a 532 nm laser. In the absorption spectra measurement, samples were excited by a L11798 deuterium lamp (Hamamatsu), and background data and transmitted light signal were collected through a position-invariant optical fiber and then detected by a QE65 Pro spectrometer from Oceano Optics Co. Ltd. In the PL spectra measurement, the samples were excited by a 193 nm light source produced by Gam Laser EX5/250-478 ArF excimer laser. The luminescent signals were first collected from the back by an optical fiber and then detected by the QE65 Pro spectrometer.

Device fabrication

A thin layer of Pt (~15–20 nm) was taken as a translucent

anode and sputtered on the top of the single crystal. The transmittance of Pt electrode is between 60% and 70% (see Supplementary Fig. S1). A glass substrate evaporated with Au metal was in contact with the bottom of a crystal cathode which was also sputtered with Pt through silver paste.

Optoelectronics measurements

The devices were placed in a Lake Shore vacuum variable temperature probe station and measured on 4200A-SCS source meter (Keithley) by Clarius software during the tests on I-V characteristics, temporal response, variable power, and variable temperature. The radiation of 228 nm and 185 nm was obtained by a L11798 deuterium lamp (Hamamatsu) and band-pass filters. Variable optical power was achieved through attenuators. Variable power and temperature were achieved by attenuators and heating function of the probe station, respectively. A VXUV20A photodetector was applied to calibrate the optical power. Spectral response measurements used a self-assembled vacuum system. During the test, these devices were placed on a miniature probe station in a vacuum chamber. Monochromatic light was obtained by a deuterium lamp and a McPherson 302 vacuum monochromator. The electrical signal of the device was read out by a Keithley 6517B source meter. The transient voltage signal test used a self-assembled pulse response test system, including a miniature probe station, a 2636B source meter (Keithley) for applying bias, a 193 nm ArF excimer laser as a light source, and a Keysight DSOS604A 6G oscilloscope for reading voltage signals. Imaging tests used a low-pressure mercury lamp and a 222 nm excimer lamp as light sources, during which the device was placed on a micro-probe stage of a two-dimensional displacement stage controlled by an SC300 displacement control box. The photosensitive area of 500 μm × 500 μm was achieved through a physical mask.

References

1. Konstantatos G, Sargent EH. Nanostructured materials for photon detection. *Nat Nanotechnol* **5**, 391–400 (2010).
2. de Arquer FPG, Armin A, Meredith P, Sargent EH. Solution-processed semiconductors for next-generation photodetectors. *Nat Rev Mater* **2**, 16100 (2017).
3. Lee W, Liu Y, Lee Y, Sharma BK, Shinde SM et al. Two-dimensional materials in functional three-dimensional architectures with applications in photodetection and imaging. *Nat Commun* **9**, 1417 (2018).
4. Lukac R. Single-sensor imaging in consumer digital cameras: a survey of recent advances and future directions. *J Real-Time Image Proc* **1**, 45–52 (2006).
5. Dai Y, Jia KP, Zhu GH, Li H, Fei Y et al. All-fiber device for single-photon detection. *PhotoniX* **4**, 7 (2023).
6. Armin A, Hambsch M, Kim IK, Burn PL, Meredith P et al. Thick junction broadband organic photodiodes. *Laser Photonics Rev* **8**, 924–932 (2014).
7. Zou HY, Li XG, Peng WB, Wu WZ, Yu RM et al. Piezo-phototronic effect on selective electron or hole transport through depletion region of vis–NIR broadband photodiode. *Adv Mater* **29**, 1701412 (2017).
8. Zhao ZJ, Xu CY, Niu LB, Zhang XL, Zhang FJ. Recent progress on broadband organic photodetectors and their applications. *Laser Photonics Rev* **14**, 2000262 (2020).
9. Li ZW, Yang W, Huang M, Yang X, Zhu CG et al. Light-triggered interfacial charge transfer and enhanced photodetection in CdSe/ZnS quantum dots/MoS2 mixed-dimensional phototransistors. *Opto-Electron Adv* **4**, 210017 (2021).
10. Yan SQ, Zuo Y, Xiao SS, Oxenløwe LK, Ding YH. Graphene photodetector employing double slot structure with enhanced responsivity and large bandwidth. *Opto-Electron Adv* **5**, 210159 (2022).
11. Armin A, Jansen-van Vuuren RD, Kopidakis N, Burn PL, Meredith P. Narrowband light detection via internal quantum efficiency manipulation of organic photodiodes. *Nat Commun* **6**, 6343 (2015).
12. Lin QQ, Armin A, Burn PL, Meredith P. Filterless narrowband visible photodetectors. *Nat Photonics* **9**, 687–694 (2015).
13. Juntunen MA, Heinonen J, Vähänissi V, Repo P, Valluru D et al. Near-unity quantum efficiency of broadband black silicon photodiodes with an induced junction. *Nat Photonics* **10**, 777–781 (2016).
14. Gao Y, Cansizoglu H, Polat KG, Ghandiparsi S, Kaya A et al. Photon-trapping microstructures enable high-speed high-efficiency silicon photodiodes. *Nat Photonics* **11**, 301–308 (2017).
15. Wang BH, Mu JF. High-speed Si-Ge avalanche photodiodes. *PhotoniX* **3**, 8 (2022).
16. Zheng ZY, Luo Q, Xu KK et al. All-silicon PIN photodetector based on black silicon microstructure. *Opto-Electron Eng* **48**, 200364 (2021).
17. Xu T, Wu YK, Luo XG, Guo LJ. Plasmonic nanoresonators for high-resolution colour filtering and spectral imaging. *Nat Commun* **1**, 59 (2010).
18. Yokogawa S, Burgos SP, Atwater HA. Plasmonic color filters for CMOS image sensor applications. *Nano Lett* **12**, 4349–4354 (2012).
19. Kim JH, Liess A, Stolte M, Krause AM, Stepanenko V et al. An efficient narrowband near-infrared at 1040 nm organic photodetector realized by intermolecular charge transfer mediated coupling based on a squaraine dye. *Adv Mater* **33**, 2100582 (2021).
20. Fang YJ, Dong QF, Shao YC, Yuan YB, Huang JS. Highly narrowband perovskite single-crystal photodetectors enabled by surface-charge recombination. *Nat Photonics* **9**, 679–686 (2015).
21. Hou YC, Wu CC, Huang X, Yang D, Ye T et al. Self-powered Red/UV narrowband photodetector by unbalanced charge carrier transport strategy. *Adv Funct Mater* **31**, 2007016 (2021).
22. Xie C, Lu XT, Tong XW, Zhang ZX, Liang FX et al. Recent progress in solar-blind deep-ultraviolet photodetectors based on inorganic ultrawide bandgap semiconductors. *Adv Funct Mater* **29**, 1806006 (2019).

23. Jia LM, Zheng W, Huang F. Vacuum-ultraviolet photodetectors. *PhotoniX* **1**, 22 (2020).
24. Zheng W, Jia LM, Huang F. Vacuum-ultraviolet photon detections. *iScience* **23**, 101145 (2020).
25. Liu C, Eschen W, Loetgering L, Penagos Molina DS, Klas R et al. Visualizing the ultra-structure of microorganisms using tabletop extreme ultraviolet imaging. *PhotoniX* **4**, 6 (2023).
26. Wilks J, Wilks E. *Properties and Applications of Diamond* (Butterworth-Heinemann, Oxford, 1991).
27. Lu YJ, Lin CN, Shan CX. Optoelectronic diamond: growth, properties, and photodetection applications. *Adv Opt Mater* **6**, 1800359 (2018).
28. Liao MY. Progress in semiconductor diamond photodetectors and MEMS sensors. *Funct Diamond* **1**, 29–46 (2021).
29. Neamen DA. *Semiconductor Physics and Devices*: *Basic Principles* (McGraw-Hill, Boston, 2003).
30. Kawarada H, Matsuyama H, Yokota Y, Sogi T, Yamaguchi A et al. Excitonic recombination radiation in undoped and boron-doped chemical-vapor-deposited diamonds. *Phys Rev B* **47**, 3633–3637 (1993).
31. Nebel CE. Electronic properties of CVD diamond. *Semicond Sci Technol* **18**, S1–S11 (2003).
32. Moram MA, Vickers ME. X-ray diffraction of III-nitrides. *Rep Prog Phys* **72**, 036502 (2009).
33. Hull D, Bacon DJ. *Introduction to Dislocations* 4th ed (Butterworth-Heinemann, Oxford, 2001).
34. Solin SA, Ramdas AK. Raman spectrum of diamond. *Phys Rev B* **1**, 1687–1698 (1970).
35. Saidaminov MI, Haque A, Savoie M, Abdelhady AL, Cho N et al. Perovskite photodetectors operating in both narrowband and broadband regimes. *Adv Mater* **28**, 8144–8149 (2016).
36. Wang J, Xiao S, Qian W, Zhang K, Yu J et al. Self-driven perovskite narrowband photodetectors with tunable spectral responses. *Adv Mater* **33**, 2005557 (2021).
37. Li JZ, Wang J, Ma JQ, Shen HZ, Li L et al. Self-trapped state enabled filterless narrowband photodetections in 2D layered perovskite single crystals. *Nat Commun* **10**, 806 (2019).
38. Li Y, Shi ZF, Liang WQ, Wang LT, Li S et al. Highly stable and spectrum-selective ultraviolet photodetectors based on lead-free copper-based perovskites. *Mater Horiz* **7**, 530–540 (2020).
39. Cicek E, McClintock R, Cho CY, Rahnema B, Razeghi M. $Al_xGa_{1-x}N$-based back-illuminated solar-blind photodetectors with external quantum efficiency of 89%. *Appl Phys Lett* **103**, 191108 (2013).
40. Seeger K. *Semiconductor Physics*: *An Introduction* 9th ed (Springer Science, New York, 2013).
41. Koizumi S, Nebel C, Nesladek M. *Physics and Applications of CVD Diamond* (John Wiley & Sons, Weinheim, 2008).
42. Clark CD, Dean PJ, Harris PV. Intrinsic edge absorption in diamond. *Proc Roy Soc A Math Phys Eng Sci* **277**, 312–329 (1964).
43. Konishi K, Naka N. Phonon-assisted excitonic absorption in diamond. *Phys Rev B* **104**, 125204 (2021).
44. Cheng L, Zheng W, Zhu YM, Huang F, Wang HK et al. Anomalous blue shift of exciton luminescence in diamond. *Nano Lett* **22**, 1604–1608 (2022).
45. Cheng L, Zhu SQ, Ouyang XP, Zheng W. Bandgap evolution of diamond. *Diamond Relat Mater* **132**, 109638 (2023).
46. Okushi H, Watanabe H, Kanno S. Characteristics of excitonic emission in diamond. *Phys Status Solidi* **202**, 2051–2058 (2005).
47. Swinehart DF. The beer-lambert law. *J Chem Educ* **39**, 333 (1962).
48. Shen XC. *Semiconductor Spectra and Optical Properties* (Science Press, Beijing, 1992).
49. Konishi K, Akimoto I, Isberg J, Naka N. Diffusion-related lifetime and quantum efficiency of excitons in diamond. *Phys Rev B* **102**, 195204 (2020).
50. Walker J. Optical absorption and luminescence in diamond. *Rep Prog Phys* **42**, 1605–1659 (1979).
51. Guo FW, Yang B, Yuan YB, Xiao ZG, Dong QF et al. A nanocomposite ultraviolet photodetector based on interfacial trap-controlled charge injection. *Nat Nanotechnol* **7**, 798–802 (2012).
52. Fox BA, Hartsell ML, Malta DM, Wynands HA, Kao CT et al. Diamond devices and electrical properties. *Diamond Relat Mater* **4**, 622–627 (1995).
53. Buonanno M, Ponnaiya B, Welch D, Stanislauskas M, Randers-Pehrson G et al. Germicidal efficacy and mammalian skin safety of 222-nm UV light. *Radiat Res* **187**, 493–501 (2017).

Acknowledgements

We are grateful for financial supports from Natural Science Foundation of Guangdong Province for Distinguished Young Scholars (Grant No. 2021B1515020105).

Author contributions

All authors commented on the manuscript. W Zheng conceived of and directed this work. LM Jia fabricated the heterojunction device and performed materials characterization and optoelectronics measurements. LM Jia, L Cheng and W Zheng analyzed the experimental results. LM Jia was mainly responsible for data analysis and preparing the manuscript.

Competing interests

The authors declare no competing financial interests.